3-2019

On the Limited Role of Electronic Support Effects in Selective Alkyne Hydrogenation: A Kinetic Study of Au/MO_X Catalysts Prepared from Oleylamine-Capped Colloidal Nanoparticles

James E. Bruno
Trinity University, jbruno@trinity.edu

K. B. Sravan Kumar

Nicolas S. Dwarica
Trinity University, ndwarica@trinity.edu

Alexander Hüther
Trinity University, ahuther@trinity.edu

Zhifeng Chen

See next page for additional authors

Repository Citation

Bruno, J. E., Sravan Kumar, K. B., Dwarica, N. S., Hüther, A., Chen, Z., Guzman, C. S., IV, Hand, E. R., ... & Chandler, B. D. (2019). On the limited role of electronic support effects in selective alkyne hydrogenation: A kinetic study of Au/MO_X catalysts prepared from oleylamine-capped colloidal nanoparticles. *ChemCatChem, 11*(6), 1650-1664. https://doi.org/10.1002/cctc.2018

Authors

James E. Bruno, K. B. Sravan Kumar, Nicolas S. Dwarica, Alexander Hüther, Zhifeng Chen, Clemente S. Guzman IV, Emily R. Hand, William C. Moore, Robert M. Rioux, Lars C. Grabow, and Bert D. Chandler

ChemPubSoc Europe
DOI: 10.1002/cctc.201801882
CHEMCATCHEM
Full Papers

On the Limited Role of Electronic Support Effects in Selective Alkyne Hydrogenation: A Kinetic Study of Au/MO$_x$ Catalysts Prepared from Oleylamine-Capped Colloidal Nanoparticles

James E. Bruno,[a] K. B. Sravan Kumar,[b] Nicolas S. Dwarica,[a] Alexander Hüther,[a] Zhifeng Chen,[c] Clemente S. Guzman IV,[a] Emily R. Hand,[a] William C. Moore,[a] Robert M. Rioux,[c, d] Lars C. Grabow,[b] and Bert D. Chandler*[a]

We report a quantitative kinetic evaluation and study of support effects for partial alkyne hydrogenation using oleylamine-capped Au colloids as catalyst precursors. The amine capping agents can be removed under reducing conditions, generating supported Au nanoparticles of ~2.5 nm in diameter. The catalysts showed high alkene selectivity (>90%) at all conversions during alkyne partial hydrogenation. Catalytic activity, observed rate constants, and apparent activation energies (25–40 kJ/mol) were similar for all Au catalysts, indicating support effects are relatively small. Alkyne adsorption, probed with FTIR and DFT, showed adsorption on the support was associated with hydrogen-bonding interactions. DFT calculations indicate strong alkyne adsorption on Au sites, with the strongest adsorption sites at the metal-support interface (MSI). The catalysts had similar hydrogen reaction orders (0.7–0.9), and 1-octyne reaction orders (~−0.2), suggesting a common mechanism. The reaction kinetics are most consistent with a mechanism involving the non-competitive activated adsorption of H_2 on an alkyne-covered Au surface.

Introduction

The selective hydrogenation of alkynes, dienes, and dialkenes in polyolefin feedstocks is a vital process to the plastics industry. These impurities, typically <5% of the feed, must be reduced to <5 ppm to prevent deactivation of the downstream polymerization catalyst. Care must be taken to prevent the over-hydrogenation of both the alkynes and the alkene feed into alkanes. Within this class of reactions, selective (or partial) acetylene hydrogenation is the most thoroughly studied due to its industrial importance in polyethylene production;[1,2] additional compounds commonly studied include 1-propyne,[3] 1,3-butadiene,[4] 1-hexyne,[5] and phenylacetylene.[6]

Monometallic Pt, Pd, and Ni catalysts have been extensively studied for selective or partial alkyne hydrogenation.[7–10] However, these metals generally have low alkene selectivity due to over-hydrogenation to alkanes and oligomerization; the generation of oligomers ("green oil") also results in catalyst deactivation. These metals are typically used in combination with less-active metals, either as an alloy (e.g. PdAg alloys) or as an electronic modifier (Au@Ni core-shell nanoparticles).[11,12] Several recent studies have also reported single atom alloys of Pd which exhibit high alkene selectivity.[11,13–17]

Gold catalysts are attractive alternatives to Pd-based materials due to thehigh intrinsic alkene selectivity of Au (~90% alkenes in the products).[18,19] Density functional theory (DFT) calculations from Segura *et al.* offer the following explanation for this unique selectivity. Acetylene and ethylene bind relatively strongly to Pd(111) ($\Delta E = -1.86$ and -0.86 eV, respectively), so the initial hydrogenation product, ethylene, binds strongly enough and has a sufficiently low barrier to undergo further hydrogenation to ethane.[20] In contrast, using a Au$_{19}$ cluster DFT model, Segura *et al.* found acetylene had a reasonable binding energy to the cluster (-0.67 eV), while ethylene binds very weakly (-0.01 eV). Thus, the barrier to desorption from Au is likely lower than the barrier to further hydrogenation.[20] However, Au is relatively poor at hydrogen activation,[21] requiring process temperatures greater than 200 °C for acceptable alkyne conversion.[22–25] Gold catalysts also lose activity within 12–24 h at operating temperatures between 180–400 °C.[18,24,25]

Partial alkyne hydrogenation over supported Au catalysts has been evaluated for a variety of feedstocks.[3,4,22,25] Much of

---

[a] Dr. J. E. Bruno, N. S. Dwarica, A. Hüther, C. S. Guzman IV, E. R. Hand, W. C. Moore, Prof. Dr. B. D. Chandler
Department of Chemistry
Trinity University
One Trinity Place, San Antonio, Texas 78240 (USA)
E-mail: bert.chandler@trinity.edu
[b] K. B. Sravan Kumar, Prof. Dr. L. C. Grabow
Department of Chemical and Biomolecular Engineering
University of Houston
Houston, Texas 77204 (USA)
[c] Dr. Z. Chen, Prof. Dr. R. M. Rioux
Department of Chemical Engineering
The Pennsylvania State University
University Park, Pennsylvania 16802 (USA)
[d] Prof. Dr. R. M. Rioux
Department of Chemistry
The Pennsylvania State University
University Park, Pennsylvania 16802 (USA)

Supporting information for this article is available on the WWW under https://doi.org/10.1002/cctc.201801882

the alkyne partial hydrogenation literature describes the manipulation of process variables such as reactor temperature and H_2/alkyne feed ratios to achieve high alkene selectivity.[23,24] Few studies report detailed kinetic analyses or explore the underlying chemistry of alkyne hydrogenation. Hydrogen activation is often cited as the rate-determining step in Au-catalyzed hydrogenation.[4,22,25–27] There is also evidence suggesting that H_2 adsorption on Au may have a lower activation barrier at the metal-support interface (MSI).[28] While electronic modification of the Au nanoparticle (NP) by the support may impact H_2 activation,[29] there is disagreement in the literature on the importance of electronic support effects. Several studies claim that activity differences between several Au/MO_x (metal oxide) catalysts were due to "support effects," but differences in rate were not quantified under differential conversion.[30,31] Other studies observed almost no difference in reactivity between Au/MO_x catalysts.[4,25] In this case, the authors hypothesized H_2 activation takes place on low-coordinated Au sites on the NP surface rather than at the MSI.[4,25] Fujitani *et al.* also predicted electronic support effects for H_2 activation on Au were so weak as to be negligible.[28]

Support effects are best studied using Au/MO_x catalysts that have structurally similar Au NPs. In deposition-precipitation methods, which are often used to prepare Au catalysts, the Au precursor deposition and the particle growth steps are intimately tied to the surface chemistry of the support. These syntheses are sensitive, so even minor variations in catalyst reaction conditions or synthesis parameters can produce significantly different particle properties. Additionally, deposition-precipitation methods for Au precursors are inappropriate for acidic supports such as silica.

Depositing colloidal NPs mitigates these issues by (i) employing solution Au NP syntheses that can be highly reproducible and (ii) allowing the use of the same solution of NPs for multiple supported catalysts.[32–34] This procedure separates NP preparation chemistry from the surface chemistry of the support, enabling the synthesis of uniform Au catalysts across a variety of supports. However, colloidal templates or capping agents must be removed with a thermal treatment under a reactive atmosphere. Capping agent removal can be challenging, and it can be difficult to prove that the capping agents are completely removed. This is particularly true for Au catalysts because the oxidative treatments that are typically employed may leave behind surface carbonates or other residues which may poison catalytically active sites.[35,36]

Our goals were to synthesize colloidal Au/MO_x catalysts (c-Au/MO_x), quantify the support effects, and evaluate the reaction mechanism. We used oleylamine-capped colloids as catalyst precursors and removed the capping agents under a reductive atmosphere. Using 1-octyne hydrogenation as a model reaction, support effects were examined both with light-off curves and differential kinetic measurements. We evaluated several common hydrogenation mechanisms in the context of our kinetic results in order to provide insight into the possible reaction pathways.

Results

Colloid and Catalyst Synthesis

A wide variety of colloidal nanoparticle stabilizers have been used to prepare heterogeneous catalysts, including polyvinylpyrrolidone (PVP) and polyvinylalcohol (PVA) polymers,[32,36–40] dendrimers,[41–45] and thiols.[46–48] These syntheses are generally performed in water or alcoholic solvents, and usually require an oxidative thermal treatment to break down the colloid stabilizer into more volatile species. Thiol capping agents can be used in non-aqueous syntheses,[46–48] but residual sulfur is similarly difficult to remove from Au.[48] We therefore sought to develop catalyst syntheses using more volatile long-chain amine capping agents.

We adapted the synthesis developed by Peng *et al.*, which uses oleylamine as a colloid stabilizer/capping agent.[49] This inexpensive and commercially available capping agent has the primary advantage of a sufficiently low boiling point (364 °C) to potentially allow for direct removal via evaporation without breaking down the capping agents into oxidized fragments that adsorb strongly onto the catalyst. This synthesis is readily scalable and can be used to prepare several grams of catalyst. Briefly, auric acid is dissolved in a tetralin-oleylamine solution and reduced with borane tert-butylamine. The nanoparticles can then be purified by precipitation with acetone and resuspended in hexanes for deposition onto catalyst supports (refer to the Experimental section for specific details). This method allows a single batch of nanoparticles to be deposited onto several different supports by simply dividing the resuspended NP solution into several parts.

Oleylamine-capped Au NPs were deposited onto three oxide supports (TiO_2, Al_2O_3, SiO_2) via spontaneous adsorption from the same batch of NPs. Oleylamine was removed by heating in flowing H_2/N_2 at 300 °C for 2 h; at this temperature, the oleylamine vapor pressure is ~300 Torr. Attenuated total reflection Fourier transform infrared spectroscopy (ATR-FTIR) confirmed removal of the capping agent (Figures S1 and S2). This is a much shorter thermal treatment than was required for thiol-capped nanoparticles.[48,50] In the thiol system, the C–S bond breaks at ~275 °C and long treatment times are required to remove the residual sulfur.[48]

Characterization of Au/MO_x Catalysts

The catalysts were initially characterized with N_2 physisorption, ICP-OES, and TEM (Table 1). The Au loading was consistent, varying between 1.1 and 1.3 wt.%. TEM micrographs for c-Au/Al_2O_3 and c-Au/TiO_2 are shown in Figure 1 (the "c-" prefix denotes a catalyst synthesized with the colloidal method). TEM measurements showed Au nanoparticles to be the same (2–3 nm) within reasonable experimental errors (Table 1). XRD data were also collected for c-Au/Al_2O_3 and c-Au/SiO_2; the Al_2O_3 support exists mostly as γ-Al_2O_3 (Figure S3A), and SiO_2 matched the reference spectra (Figure S3B). No Au reflections were observed in the XRD spectra for c-Au/Al_2O_3 and SiO_2, indicating

Table 1. Characterization Data for Au/MO_x Catalysts.

Catalyst	wt.% Au	Surface area support [m^2/g]	Surface area catalyst [m^2/g]	Particle diameter [nm]
Pd/Al_2O_3[a]	0.3 (Pd)	n/a	110	>50
Au/TiO_2[b]	1.0	n/a	55	4.1 ± 2.2
c-Au/TiO_2	1.2	30	45	2.5 ± 1.5
c-Au/SiO_2	1.1	300	260	3.2 ± 1.1
c-Au/Al_2O_3	1.3	140	80	1.9 ± 1.0

[a] Vanguard Catalyst (0.3 wt.% Pd/Al_2O_3); [b] Haruta Gold International (HGI).

the Au particles were <4 nm. The HGI Au/TiO_2 had similar Au loading and surface area to the synthesized Au/TiO_2, but the Au particle sizes were slightly larger with a broader distribution.

To examine a more reducible support, we also prepared, characterized, and tested a c-Au/Fe_2O_3 catalyst. In the absence of Au colloids, the reductive treatment used to remove the oleylamine capping agents was found to cause significant support reduction, generating large Fe(0) particles. A comparison of the characterization, catalytic activity, and kinetics of c-Au/Fe_2O_3 to the other c-Au/MO_x catalysts is found in the SI (Figures S4-S8, Tables S1-S2).

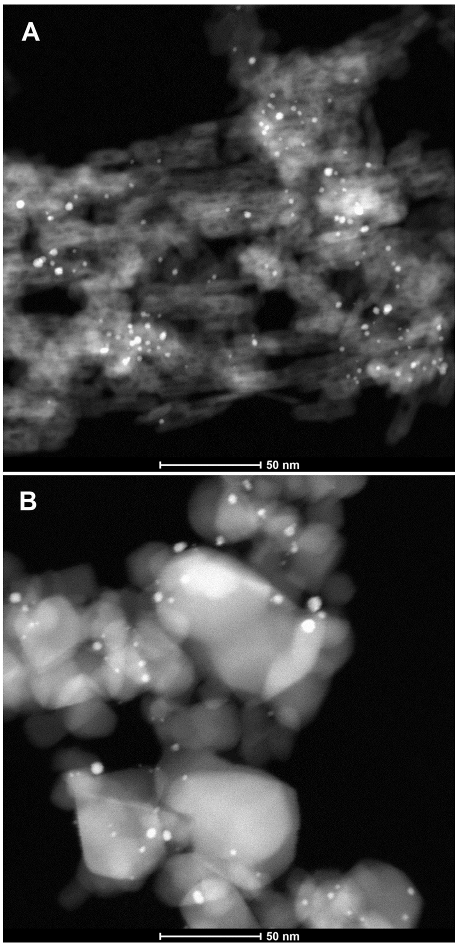

Figure 1. TEM micrographs for 1.3 wt.% c-Au/Al_2O_3 (A) and 1.2 wt.% c-Au/TiO_2 (B).

Light-off Curves

Light-off curves were used to evaluate gross catalytic behavior activity and examine selectivity over a wide range of conversion (Figure 2A). Several conclusions arise from these data. First, the reaction profile for c-Au/TiO_2 was essentially the same as the commercial catalyst synthesized by deposition/precipitation (HGI Au/TiO_2; see Figures 2 and S9). The colloidal synthesis yield catalysts that are appropriate models for traditionally prepared catalysts. Additionally, there does not appear to be deleterious effects from the colloid synthesis and capping agent removal.

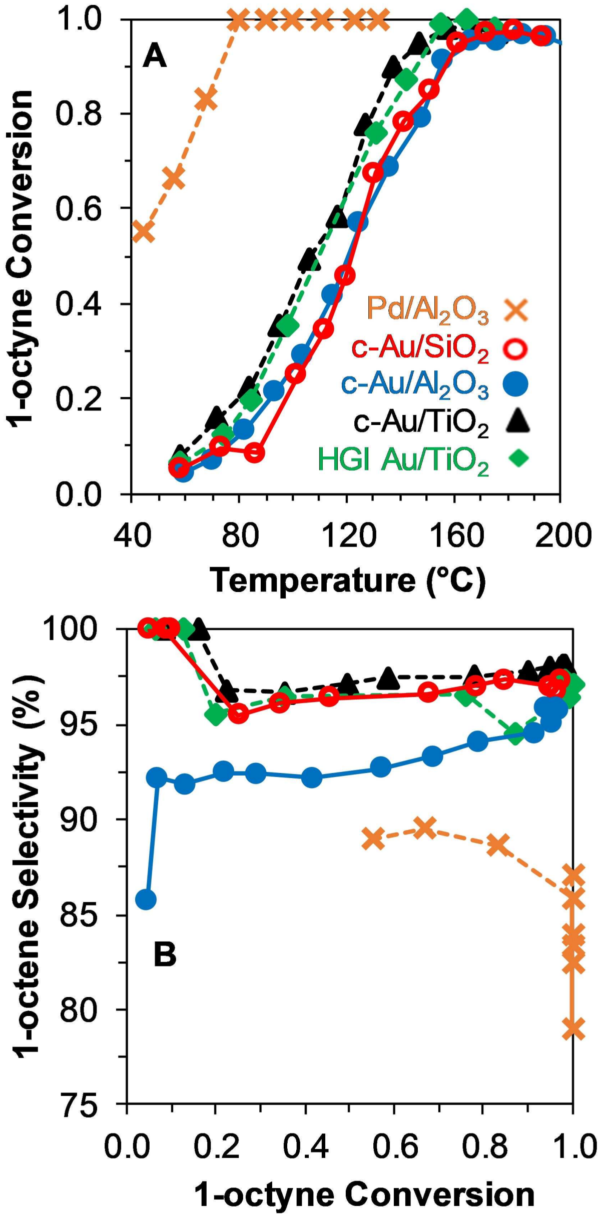

Figure 2. 1-Octyne hydrogenation screening data. (A) Conversion versus temperature light-off curves; (B) 1-octene selectivity versus conversion plots, extracted from the light-off curve data. Details on the commercial Pd/Al_2O_3 catalyst are available in the SI. Conditions: 50 mL/min H_2, 20 Pa 1-octyne, 5–7 mg catalyst, GHSV = ~9700 h^{-1}.

Second, the light-off curves for all colloidal catalysts were very similar, with the T_{50} varying by about ±10 °C. Finally, an additional c-Au/Al_2O_3 catalyst was prepared from a separate batch of Au colloids and had a loading of 1.1 wt.% Au. The colloidal synthesis showed excellent batch-to-batch reproducibility, as the light-off curves for the two catalysts had only minor differences attributable to the slightly different Au loadings (Figure S10).

Figure 2B shows selectivity versus conversion plots from the light-off curve data. The Au catalyst selectivity to 1-octene was >90% at all measures of 1-octyne conversion. Our results with 1-octyne are consistent with previous studies examining 1,3-butadiene hydrogenation over Au catalysts.[4,25,30] The lack of support effects in the synthesized catalysts is somewhat surprising, given the widely attributed importance of metal-support interactions in the literature.[51–54]

These trends highlight one of the potential advantages of Au-based partial hydrogenation catalysts: they are inherently more selective to 1-octene than traditional hydrogenation catalysts (e.g. Ni, Pd, Pt). As is often the case, higher selectivity comes at the price of reduced activity. This tradeoff is most obvious at the highest conversions, highlighted by the inset plot in Figure 2B. For Pd/Al_2O_3, the alkene selectivity drops after the temperature surpasses 80 °C (T_{100}) and the catalyst over-hydrogenates alkenes into alkanes. This indicates alkene adsorption and hydrogenation are competitive with alkyne adsorption and hydrogenation when there relatively little alkyne present. The Au catalysts, on the other hand, maintained high alkene selectivity at temperatures higher than those required for 100% conversion.

Adsorption of 1-Octyne to Au/MO_x and MO_x

To better understand the underlying chemistry, we examined 1-octyne adsorption on the three c-Au/MO_x catalysts and their supports using *in-situ* FTIR spectroscopy. The results for Al_2O_3 and c-Au/Al_2O_3 are presented in Figure 3. The FTIR spectra contain three primary areas of interest: the triple bond stretch (–C≡C–, 2127 cm^{-1}), the alkynyl C–H stretch (H–C≡C, 3320 cm^{-1}), and the –OH stretching region on the supports (~3700 cm^{-1}). FTIR spectra of Al_2O_3 under a flow of 1-octyne show a modest red shift in the –C≡C– stretch from 2127 to 2110 cm^{-1} upon adsorption (Figure 3A). A similar red shift was observed for the band attributed to the terminal alkynyl C–H stretch, which shifted from 3320 cm^{-1} to 3280 cm^{-1} (Figure 3B). These shifts coincided with changes in the support -OH groups. When 1-octyne was added to the system, the intensity of the "dangling OH" groups (non-hydrogen-bonded OH groups) decreased significantly. This is accompanied by an increase in the broad H-bonded O–H stretch at ~3550 cm^{-1} and broadening of the alkyne terminal hydrogen stretch at 3280 cm^{-1} (Figure 3B). Considered together, all of these changes are consistent with hydrogen bonding between the alkynyl proton and surface hydroxyls. The weakening of the –C≡C– bond is partly attributed to electron donation from the alkyne moiety to –OH protons on the Al_2O_3 support. Similar interactions were also reported for 1-propyne adsorption on Pd/ZrO_2.[55] These experiments were repeated on TiO_2 and SiO_2 supports (Figure S11A and S12 A); in both cases, the IR spectra show similar shifts in the –OH, H–C≡C, and –C≡C– regions, so this adsorption motif appears to be similar for the oxide supports examined in this work.

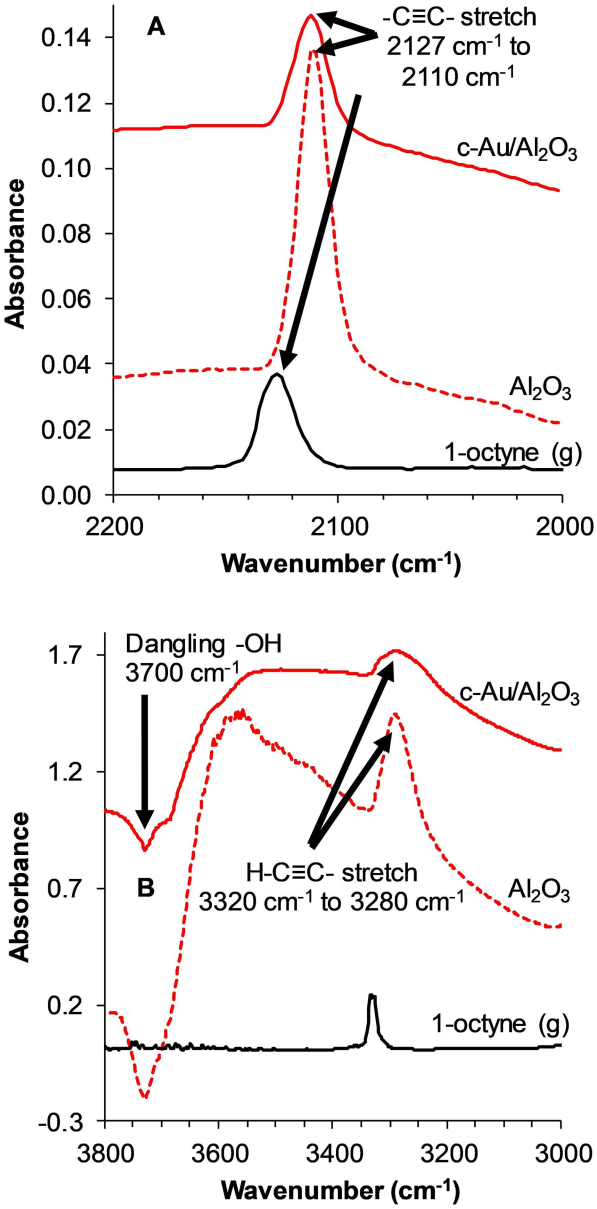

Figure 3. FTIR spectra of 1-octyne in the gas phase and adsorbed on both Al_2O_3 and c-Au/Al_2O_3. A: 2000–2200 cm^{-1}; B: 3000–3800 cm^{-1}.

Figure 3 shows FTIR spectra for 1-octyne adsorption on c-Au/Al_2O_3. The observed spectral changes upon adsorption of 1-octyne to the c-Au/Al_2O_3 catalyst were indistinguishable from the bare support. Identical 1-octyne adsorption experiments were performed on c-Au/TiO_2 and c-Au/SiO_2 (Figure S11B and S12B). The IR spectra were essentially the same as Al_2O_3 – no spectral features directly attributable to 1-octyne adsorption on Au were observed. These results are likely due to a combination

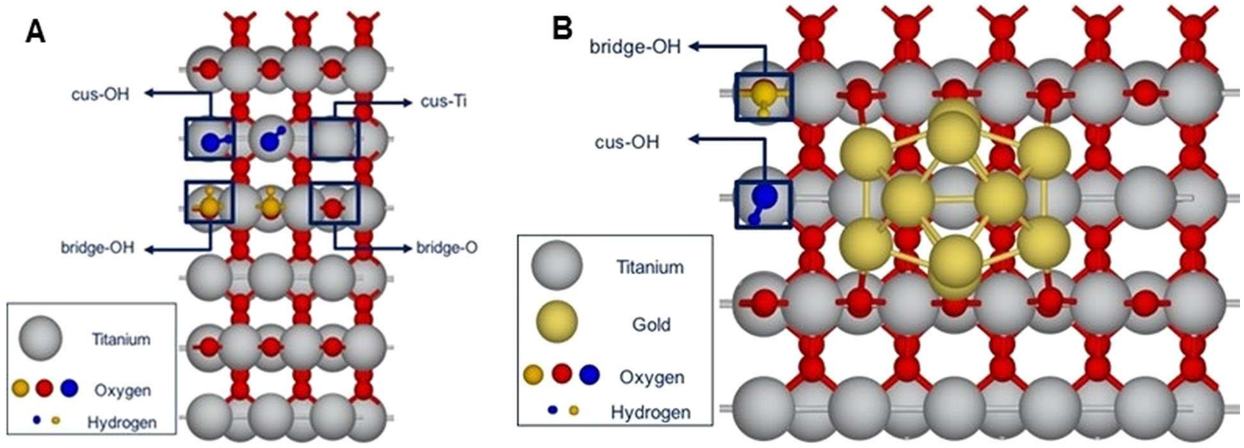

Figure 4. Top views of the (A) TiO_2 model and (B) Au/TiO_2 model using atomic radii. The two types of hydroxyl groups are differentiated by color: cus-OH (blue) and bridge-OH (orange).

of factors. First, the surface area of the support is significantly larger than the surface area of Au, so even weak adsorption on a much larger surface may conceal signals from adsorption on Au. Any changes to the C–H stretching bands upon adsorption to Au were too small to differentiate from the changes associated with adsorption on the support. Second, the surface selection rule dictates that vibrating dipoles parallel to the surface of a small metal nanoparticle (diameter >2 nm) are IR-invisible.[56,57] The metal surface generates an image dipole that cancels out the effect of the dipole change originating in the vibrating molecule.[57] The Au nanoparticles are 2–4 nm, and linear alkynes are thought to adsorb parallel to the Au surface,[58] so 1-octyne species adsorbed to Au may not be detectable with FTIR.

DFT Simulations of 1-Propyne Adsorption

Density functional theory (DFT) was used to simulate alkyne adsorption on a model support (TiO_2) and catalyst (Au/TiO_2) in order to help interpret the IR data. The computational model consists of a rutile TiO_2 (110) (3×3) unit cell separated by a vacuum space of 20 Å in the direction perpendicular to the surface (Figure 4A). The bottom two layers of TiO_2 were fixed in their bulk positions, while all other degrees of freedom were relaxed. Two water molecules were dissociated on the TiO_2(110) surface to create bridge-hydroxyl groups (bridge-OH) and hydroxyl groups at coordinatively unsaturated (cus) Ti atoms (cus-OH). The adsorption of 1-octyne is difficult to simulate because the long alkyl chain requires a much larger unit cell to avoid lateral interactions between adsorbed species in individual cells. A terminal alkyne with a smaller alkyl chain is computationally less expensive, so 1-propyne was evaluated as a model compound. We compared information from the calculated alkyne adsorption system to experimental values in order to evaluate the suitability of the DFT model system. Additional computational details can be found in the Experimental section below.

Table 2 compiles experimental and computational FTIR frequencies for the –C≡C– triple bond stretch ($\nu_{C\equiv C}$) and the terminal alkynyl C–H stretch ($\nu_{C\equiv C}$). Experimental measurements have shown $\nu_{C\equiv C}$ of 1-octyne (2127 cm^{-1}) is 15 cm^{-1} lower in energy than 1-propyne (2142 cm^{-1}).[59] The simulated $\nu_{C\equiv C}$ values are ~35 cm^{-1} higher in energy than the experimental values. However, the DFT calculated Δ $\nu_{C\equiv C}$ is 10 cm^{-1}, so the computational model does a reasonable job of reproducing the electronic differences between the two compounds, even if it does not exactly reproduce the absolute individual stretching frequencies. These effects are also reflected in the $\nu_{H-C\equiv C}$ stretching frequencies: the differences between the two molecules are similar (4 and 0 cm^{-1}, Table 2), despite DFT stretching frequencies that are ~110 cm^{-1} higher in energy.

Table 2. Experimental and simulated stretching frequencies for 1-octyne and 1-propyne in both the gas phase and adsorbed to TiO_2 hydroxyl sites.

Experimental Frequencies	$\nu_{C\equiv C}$	$\nu_{H\text{-}C\equiv C}$
1-propyne (g)[59]	2142 cm^{-1}	3334 cm^{-1}
1-octyne (g)	2127 cm^{-1}	3330 cm^{-1}
Δ (C_3–C_8) (g)	15 cm^{-1}	4 cm^{-1}
Simulated Frequencies	$\nu_{C\equiv C}$	$\nu_{H\text{-}C\equiv C}$
1-propyne (g)	2176 cm^{-1}	3443 cm^{-1}
1-octyne (g)	2166 cm^{-1}	3443 cm^{-1}
Δ (C_3–C_8) (g)	10 cm^{-1}	0 cm^{-1}
Experimental Alkyne Adsorption	$\nu_{C\equiv C}$	$\nu_{H\text{-}C\equiv C}$
1-octyne (adsTiO2)[a]	2112 cm^{-1}	3271 cm^{-1}
Δ (gas phase – adsTiO2)	15 cm^{-1}	59 cm^{-1}
Simulated Alkyne Adsorption	$\nu_{C\equiv C}$	$\nu_{H\text{-}C\equiv C}$
1-propyne (adsTiO2)	2162 cm^{-1}	3419 cm^{-1}
Δ (gas phase – adsTiO2)	13 cm^{-1}	24 cm^{-1}

[a] Relaxed geometries and energetics shown in Supporting Information Figure S8.

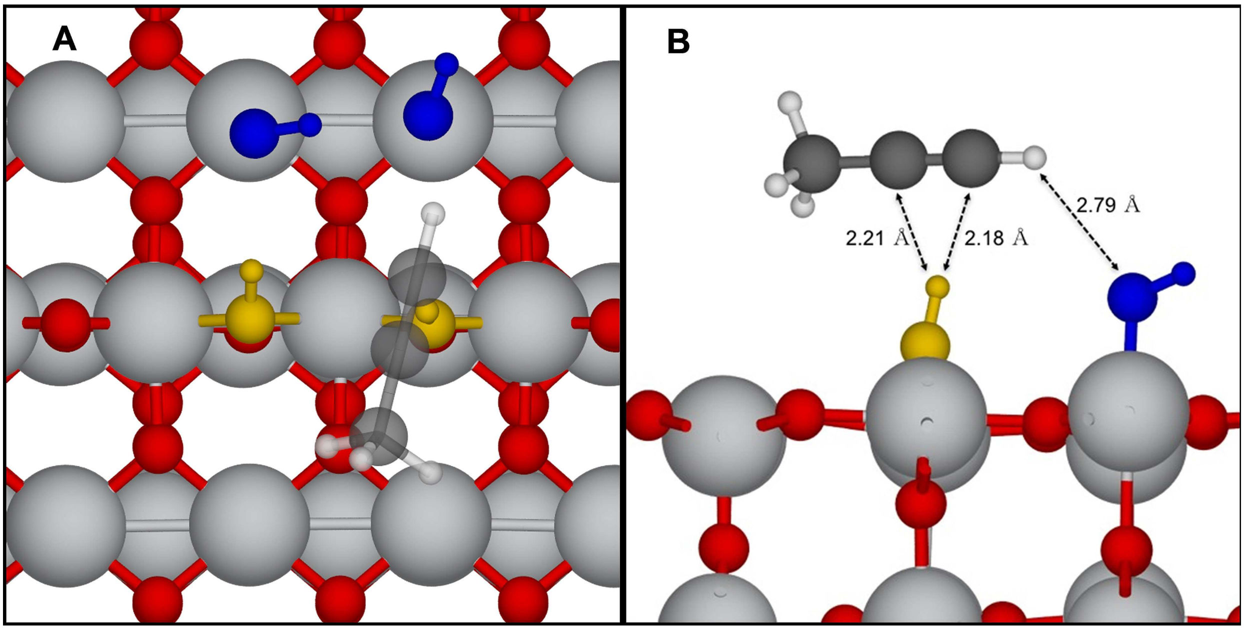

Figure 5. Simulated 1-propyne physisorption on hydroxylated TiO_2 from the top view (A) and side view (B).

Next, we simulated physisorption of 1-propyne to the hydroxylated TiO_2 surface sampling a sufficiently large space of adsorption geometries. The most stable adsorption mode (−34 kJ/mol) contains a weak hydrogen bond between the bridge-OH and the triple-bonded carbon atoms (Figure 5A). The DFT calculated $\nu_{C\equiv C}$ for physisorbed 1-propyne red-shifted by 13 cm^{-1} from the DFT-calculated gas phase value (Table 2). This weakening of the triple bond is a consequence of the electron donation to the H-bond with the surface bridge-OH group. Additionally, the distance between the proton and the center of the triple bond is about 2 Å, which is well within the range of typical distances associated with hydrogen bonding. The experimental data for 1-octyne adsorption on TiO_2 show essentially the same change in $\nu_{C\equiv C}$ upon adsorption (15 cm^{-1}, Figure S11A, Table 2).

The DFT model also showed a red shift of 24 cm^{-1} for 1-propyne $\nu_{H-C\equiv C}$ upon adsorption. This shift indicates a weakening of the terminal C–H bond due to the partial proton donation in the H-bond with the support cus-OH (Figure 5B). The experimental shift in $\nu_{H-C\equiv C}$ due to the adsorption of 1-octyne is somewhat larger (59 cm^{-1}) than the DFT prediction based on 1-propyne. These changes upon adsorption are not surprising given the large difference in calculated $\nu_{H-C\equiv C}$ values for the gas phase molecules. There may also be a greater degree of proton donation in the real system than in the simplified computational model; this would be expected if the computational model slightly underestimated the basicity of the surface hydroxyl groups. Despite these limitations, the simulated adsorption of 1-propyne to TiO_2 successfully explained the observed experimental frequency changes for 1-octyne with reasonable errors. Thus, the physisorption of 1-octyne likely occurs through the same types of H-bonding interactions identified in the DFT studies of 1-propyne adsorption.

Seven additional physisorption geometries are presented in the Supplementary Information (Figures S13–S19, Table S3). In one of these modes, we considered the possibility that a reductive pretreatment may cause partial dehydroxylation of the support, resulting in exposed cus-Ti atoms. Adsorption of the alkyne to the exposed cus-Ti atom through the triple bond is largely similar to the interactions with the bridge-OH proton (Figure S19). Adsorption to the cus-Ti site was calculated to be slightly more favorable (−44 kJ/mol) than to the Ti-OH groups (−34 kJ/mol). However, the experimental shifts observed for 1-octyne adsorption on TiO_2, Al_2O_3, and SiO_2 are all consistent, so the adsorption is more likely dominated by interactions with surface hydroxyls rather than exposed Ti atoms. The dissociative adsorption energy of water on cus-Ti atoms to form a pair of bridge-OH and cus-OH was found to be −72 kJ/mol, so residual water in the FTIR cell would rapidly quench exposed cus-Ti sites and is expected to out-compete alkynes for any exposed Ti sites.

The adsorption of 1-propyne to a supported Au NP was also studied to evaluate the possibility of alkyne adsorption to Au sites, despite these species being undetectable in IR experiments. The Au/TiO_2 model was created by placing a 10-atom Au nanocluster on a four-layer rutile TiO_2(110) slab with a (5×2) unit cell (Figure 4B). The Au nanocluster and the top two layers of TiO_2 were relaxed while the bottom two layers were fixed. Further details about this Au/TiO_2 model can be found elsewhere.[60] For simplicity, only one dissociated water molecule was used in this model. Two adsorption modes were simulated based on the predominant literature for alkyne adsorption on Au_{10} (Figures 6 and S20): the triple-bonded

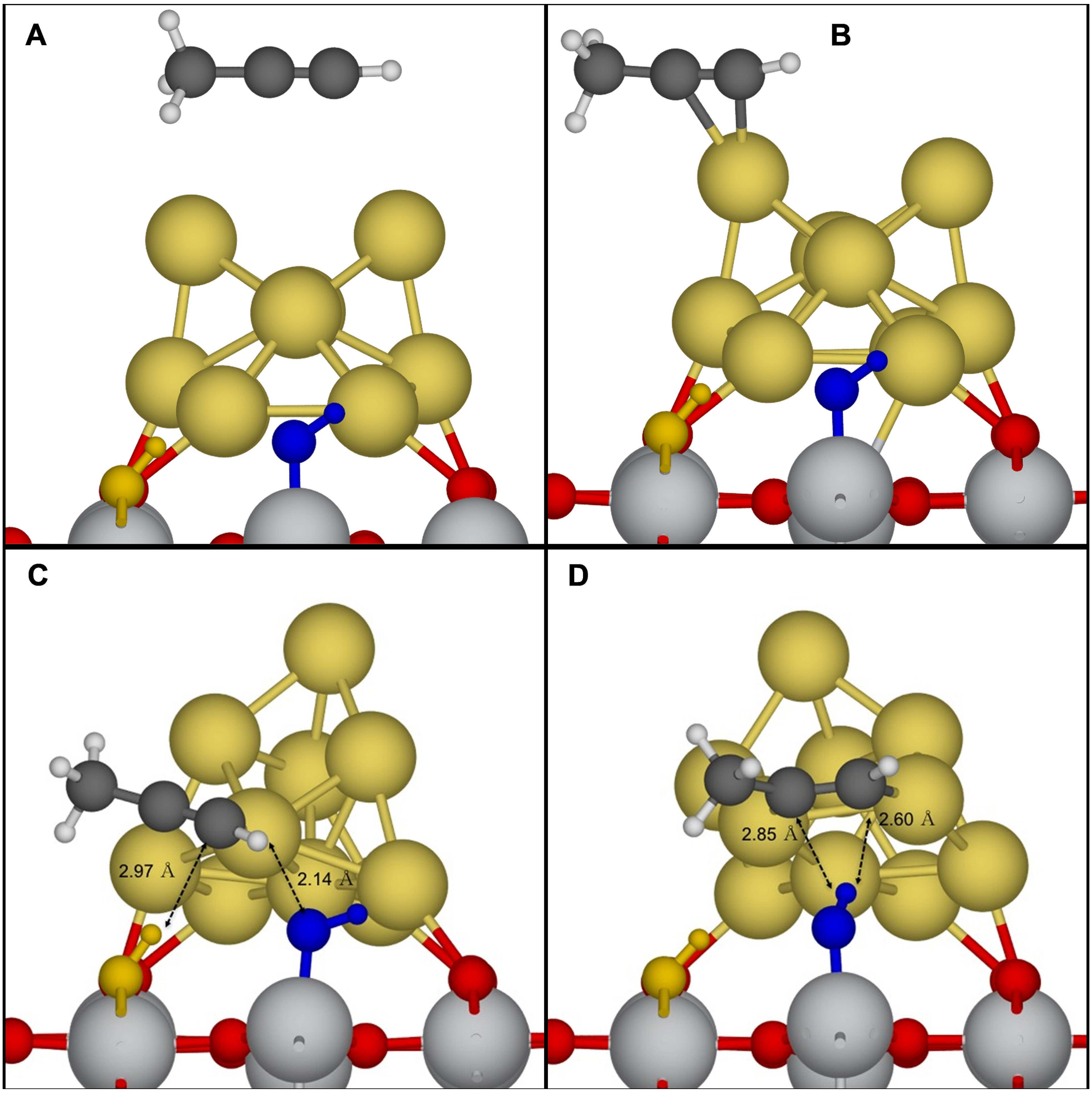

Figure 6. Simulated 1-propyne binding to Au_{10}/TiO_2, side view. (A) and (C) are di-σ orientations, (B) and (D) are π-orientations; (A) and (B) are bonded on top of the Au particle Au, (C) and (D) are bonded to Au sites at the metal-support interface.

carbon atoms bound to the same atom in Au_{10} (π-mode), or two separate atoms in Au_{10} (di-σ mode).[58]

The adsorption energies for 1-propyne on gold are presented in Table 3 and Figure 6. We note that energy contributions caused by the severe reconstruction of the Au cluster have been minimized by reporting these values with reference to the restructured geometries instead of the ordered starting geometry shown in Figure 4. Thermodynamically favorable π-and di-σ adsorption modes were identified; the π-mode of adsorption is generally preferred. The adsorption energy for the π-mode is reasonably strong on top of the particle but moderately stronger at the MSI. The stronger adsorption of the electron-donating alkyne suggests the interface Au atoms may

Table 3. Adsorption energies (in kJ/mol) of 1-propyne on Au_{10}/TiO_2 calculated using DFT.[a]

Adsorption Site	Adsorption Mode	
	di-σ	π
Top of Particle	−2	−41
Interface	−45	−85

[a] Because of the large structural rearrangement of Au atoms we report the binding energy with respect to the restructured Au clusters instead of the ordered starting geometry shown in Figure 4. The resulting binding energy is most representative of the interaction of 1-propyne with Au and not dominated by surface reconstruction energies.

be somewhat electron poor, as Haruta and coworkers postulated.[28] However, these results must be considered in the context of the model. The Au_{10} cluster likely overestimates binding energies because the individual atoms are more highly uncoordinated than in a 2–3 nm NP. Nevertheless, with the adsorption of 1-propyne on Au being stronger than both alkyne adsorption on the support (-34 to −44 kJ/mol, see above) and H_2 adsorption on Au (57 kJ/mol, see Table S22),[61] our simulations suggest that alkynes are likely present on Au sites, even if no IR fingerprint for alkyne adsorption to Au was directly observed.

We recently published a detailed study of H_2 dissociative chemisorption using a 1-D periodic nanorod model; readers are directed there for a full discussion of H_2 adsorption on Au.[61] We extended this study to include homolytic dissociation of H_2 onto the $Au_{10}/TiO_2(110)$ model (the model used above for propyne adsorption). Hydrogen adsorption on the cluster model is endothermic (57 kJ/mol, see SI) and is generally consistent with our previous calculations using the nanorod model.[61] The somewhat more favorable adsorption near the MSI for the 10-atom cluster model (57 kJ/mol) compared to the nanorod model (76 kJ/mol) can be attributed to the lower coordination number and higher mobility of Au atoms in the cluster representation. In previously published work, we also calculated barriers for homolytic H_2 dissociation on Au sites of the nanorod with local (111) and (211) configuration both directly at and away from the metal-support interface. The activation energy barrier showed little sensitivity to these sites and was consistently determined to be in the range of 105–125 kJ/mol. Given the good agreement of the calculated dissociative adsorption energies between the cluster and nanorod model, it is reasonable to assume that the activation barriers translate similarly between the two models. The DFT and IR data therefore indicate that alkyne adsorption is significantly stronger than H_2 adsorption, both on the Au nanoparticles, on the support, and at the metal-support interface. We interpret the kinetics data below in the context of these results.

Kinetic Evaluation of 1-octyne Hydrogenation

Apparent activation energy barriers (E_{app}), 1-octyne and H_2 reaction orders were determined under differential reactor conditions (Table 4). The E_{app} values for the colloidal catalysts are similar, falling in a range of 28–40 kJ/mol (Figure 7). The HGI Au/TiO_2 catalyst had a slightly larger apparent activation energy (47 ± 1 kJ/mol). Reaction orders for 1-octyne were between 0.0 and −0.3 (Figure 8A), indicating a weak inhibition by the alkyne. H_2 orders were 0.7-0.9 for the colloidal catalysts (Figure 8B), suggesting H_2 activation may be a key mechanistic step.

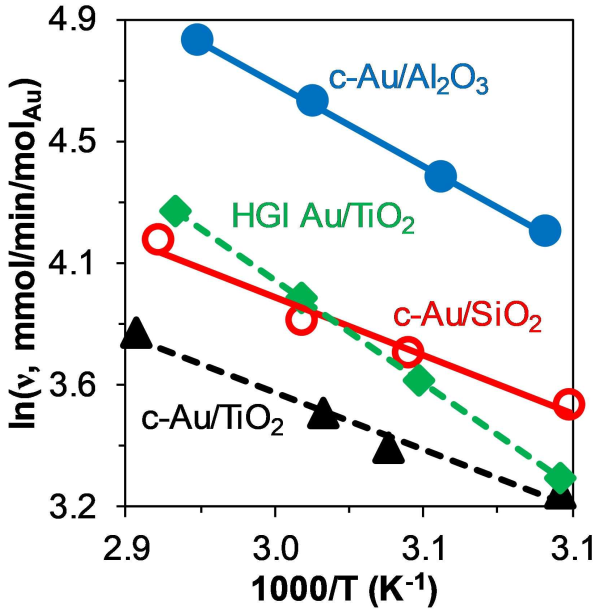

Figure 7. Arrhenius plot for the catalysts. Conditions: 45–60 °C, 50 mL/min H_2, 20 Pa 1-octyne.

Table 4. Kinetic parameters for Au/MO_x catalysts.

Catalyst	E_{app} [kJ/mol]	1-Octyne order	H_2 order	k_{obs}[c,d]
Pd/Al_2O_3[a]	21 ± 5	−0.2 ± 0.1	0.9 ± 0.1	4300 ± 1100
Au/TiO_2[b]	47 ± 1	0.0 ± 0.1	1.2 ± 0.1	4.6 ± 1.8
$c\text{-}Au/TiO_2$	26 ± 2	−0.2 ± 0.1	0.8 ± 0.1	3.6 ± 0.7
$c\text{-}Au/SiO_2$	29 ± 3	−0.3 ± 0.1	0.7 ± 0.1	6.5 ± 0.6
$c\text{-}Au/Al_2O_3$	38 ± 1	−0.2 ± 0.1	0.9 ± 0.1	3.4 ± 0.7

[a] Catalyst (0.3 wt% Pd); [b] Haruta Gold International (HGI); [c] Conditions: 50 mL/min H_2, 20 Pa 1-octyne, 60 °C; [d] k_{obs} units: mol1-octene$[1\text{-octyne}]^{0.2}$ $[H_2]^{-0.9}mol_{Au}{}^{-1}min^{-1}$.

The observed rate law is described by Equation (1).

$$\nu_{obs} = k_{obs}[H_2]^{0.9}[1-\text{octyne}]^{-0.2} \quad (1)$$

Kinetic parameters were similar for all catalysts studied, indicating alkyne hydrogenation likely proceeds by the same or similar mechanism over the various Au/MO_x catalysts. For comparison amongst catalysts, we calculated the observed rate constants from the H_2 order using an average alkyne reaction order (Table 4). As expected, the k_{obs} value for the commercial Pd/Al_2O_3 catalyst is orders of magnitude greater than for the Au catalysts. The k_{obs} values for the Au catalysts differed by a factor of 2, indicating the support plays a relatively small role in determining hydrogenation activity.

Discussion

Although several studies have explored Au-catalyzed alkyne hydrogenation and related reactions, there has been relatively little discussion of the underlying mechanisms or the role of the MSI in the reaction. For example, Hugon *et al.* studied 1,3-butadiene hydrogenation over Au, a reaction closely related to alkyne partial hydrogenation. They observed no rate differences over Au supported on Al_2O_3, TiO_2, CeO_2, and ZrO_2.[4] They concluded hydrogenation took place on the Au NP without direct participation from the support. Masoud *et al.* made

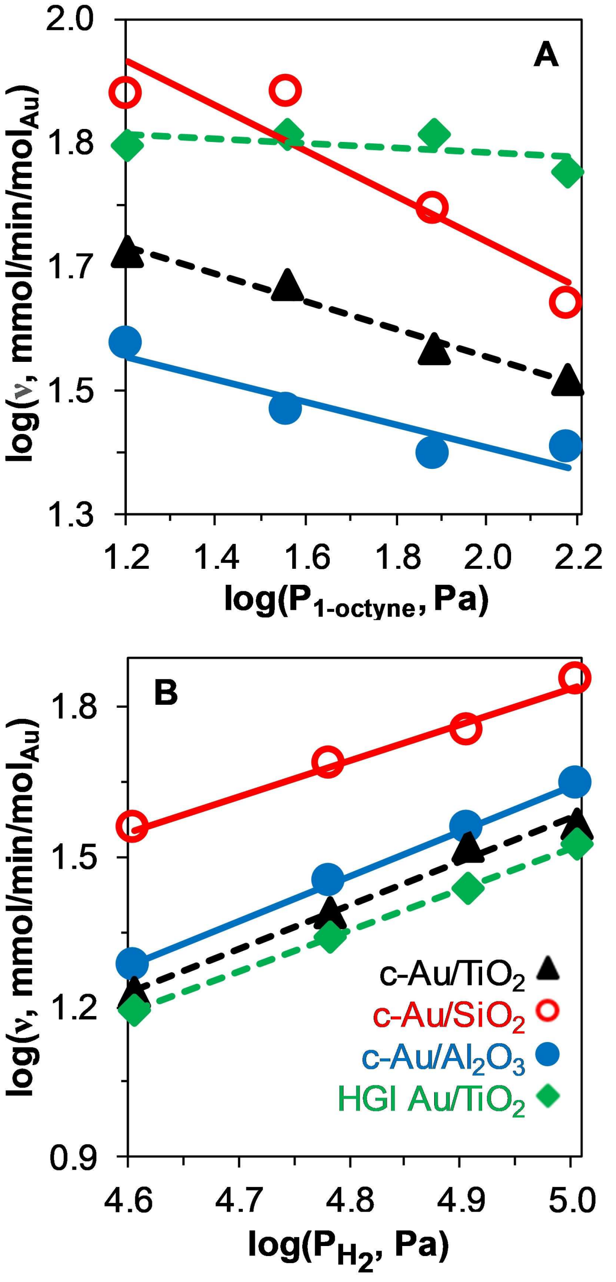

Figure 8. (A): 1-Octyne reaction order plot. Conditions: 20–200 Pa 1-octyne, 50 mL/min H_2, 60 °C. (B): H_2 reaction order plot. Conditions: 20–50 mL/min H_2, 20 Pa 1-octyne, 60 °C.

similar observations for 1,3-butadiene hydrogenation over Au/SiO_2 and Au/TiO_2.[25] Our data show a similarly small support effect: the differences in observed rate constants at 60 °C is roughly a factor of 2 (Table 4).

The mechanistic implications of the support effects in the literature were not investigated. In the following discussion, we attempt to place the results reported here into the context of the reaction kinetics measured both here and in the available alkyne hydrogenation literature. The key kinetic determinations from the Results section are (i) alkene selectivity is always high; (ii) the reaction is approximately 1st order in H_2, indicating hydrogen activation is an importantkinetic step; and (iii) the reaction has a slightly negative reaction order in alkyne, suggesting a weak competition between hydrogen and the alkyne for the active sites. Since the alkene selectivity was always high, slower oligomerization processes, which lead to "green oil", are not included in the following discussions.[25]

Discussion of Partial Alkyne Hydrogenation Mechanisms in the Literature

To our knowledge, only two mechanisms have been proposed for selective alkyne hydrogenation on Au. Azizi *et al.* proposed a simple mechanism where activated hydrogen reacts with adsorbed acetylene to form ethylene, two forms of coke, and methane.[23] Sárkány proposed a similar mechanism that also accounted for ethane formation.[62] Both mechanisms were qualitative descriptions that lacked critical analysis of the reaction kinetics. Despite the lack of formal mechanisms, the literature contains descriptions of the elementary steps necessary to build an informed mechanistic interpretation of the kinetic data collected over these new catalysts.

Kinetic studies of acetylene hydrogenation were used to measure the acetylene reaction order as 0.1 over Au/CeO_2[23] and −1.0 over Au/Al_2O_3.[19] While the Au/CeO_2 study is consistent with our data, the Au/Al_2O_3 data suggests significantly stronger alkyne inhibition than we observed. Sárkány similarly inferred strong alkyne binding to Au, hypothesizing that alkynes initially adsorbed to a majority of Au(111) and Au (100) sites and saturated the surface.[62] Corma and Sabater suggested reaction temperatures for acetylene hydrogenation needed to be >200 °C to increase the rate of H_2 activation on Au,[63] although higher temperatures are conducive for the desorption of strongly-bound alkynes.

The strong dependence on hydrogen pressure indicates H_2 binding and activation are important kinetic steps. Although there are few in-depth studies in the direct context of alkyne hydrogenation over Au, hydrogen activation over Au is of broad interest in other reactions. Two dominant active site models for H_2 activation on Au have emerged: (i) activation on the Au particle at low-coordinate corner and edge atoms[26] and (ii) at the metal-support interface.[28] Below, we examine the kinetic data in the context of several kinetic models in order to determine which mechanisms are more consistent or inconsistent with the reaction data.

Evaluation of Homolytic H_2 Activation Mechanisms

Hydrogen activation is generally assumed to occur through dissociative chemisorption, generating two Au(H) species. Pan *et al.* found that molecular hydrogen bound to high-coordinated Au(111) desorbed at ~110 K whereas hydrogen bound to Au(110) desorbed at ~220 K.[64,65] These results indicate H_2 binding to extended Au surfaces is very weak, and these surfaces are unlikely to be important in H_2 activation on supported catalysts. Bus *et al.* studied H_2 activation on Au/Al_2O_3

using H_2 chemisorption and X-ray spectroscopy techniques.[26] They concluded H_2 is activated exclusively on corner and edge Au atoms without migration to Au(111). Both Bus *et al.* and Jia *et al.* estimated that, at most, ~20% of Au sites adsorb activated hydrogen.[19,26] Based on DFT calculations and IR spectroscopy, Boronat *et al.* similarly suggested H_2 activated at low-coordinated Au–Ti sites and not interfacial Au–O sites.[66]

The Horiuti-Polanyi (H–P) mechanism has long been considered the dominant reaction mechanism for ethylene and acetylene hydrogenation on most late-transition metals.[7,8,67] After adsorption of the alkene/alkyne and dissociative chemisorption of H_2 on the metal, the H–P mechanism proceeds through two steps: (i) reversible addition of the first hydrogen to the alkyne followed by (ii) irreversible addition of the second hydrogen.[68] Non-H–P mechanisms are also possible; Yang *et al.* recently probed whether non-H–P mechanisms were relevant on low-coordinated (211) sites for Au, Pd, and Cu.[67] Hydrogenation of acetylene to ethylene on Au(211) was found to proceed primarily through the H–P mechanism, but over-hydrogenation to ethane went through a non-H–P process.[67]

Scheme 1 shows the elementary steps of the H–P mechanism applied to a supported Au catalyst, treating the system as follows: (1.1) dissociative chemisorption of H_2 (homolytic activation) on surface Au atoms; (1.2) 1-octyne adsorption on Au; (1.3) reversible addition of the first hydrogen to the octyne triple bond; and (1.4) reductive elimination of 1-octene. Due to the high observed alkene selectivity, which is consistent with weak Au-octene adsorption,[20] we treat step (1.4) as an irreversible final mechanistic step. The formal H–P mechanism considers the reductive elimination of the alkene as the rate-determining step (RDS); we consider this possibility along with other possible RDS's.

$$H_2 + 2Au \overset{K_{H_2}}{\leftrightarrow} 2Au(H) \tag{1.1}$$

$$HCCR + Au \xleftrightarrow{K_{HCCR}} Au(HCCR) \tag{1.2}$$

$$Au(H) + Au(HCCR) \overset{K_3}{\leftrightarrow} Au(H_2CC^{*}R) + Au \tag{1.3}$$

$$Au(H) + Au(H_2CC^{*}R) \overset{k_4}{\rightarrow} H_2CCHR + 2Au \tag{1.4}$$

Scheme 1. Mechanism for 1-octyne hydrogenation based on the literature; HCCR is 1-octyne and H_2CC^*R is partially-hydrogenated 1-octyne.

The RDS for Au-catalyzed hydrogenation is often reported to be the activation of H_2 (1.1).[4,22,27,69] The literature E_{app} values for H_2 activation at perimeter Au/TiO_2 sites are 30–40 kJ/mol.[26,28] These values are similar to literature E_{app} values for acetylene hydrogenation over Au/Al_2O_3 (28–42 kJ/mol) and Au/CeO_2 (37 kJ/mol).[18,22,23] Most studies conclude H_2 activation is rate-limiting due to E_{app} barriers in the 30–40 kJ/mol range with positive H_2 reaction orders. Our E_{app} barriers, reported in Table 4 (~25–40 kJ/mol), are also consistent with the cited measurements. In prior work we used a 1D periodic Au nanorod model on TiO_2 to calculate intrinsic activation barriers for homolytic H_2 dissociation over Au sites and obtained values between 105–125 kJ/mol.[61] However, if dissociative H_2 chemisorption is rate-determining, then the overall reaction rate is described by Equation (2). The full derivations are available in the SI.

$$\nu_{rxn} = \frac{\sqrt{K_{H_2} P_{H_2}}[Au]_T}{K_{HCCR} P_{HCCR}} \tag{2}$$

The maximum possible H_2 reaction order for a reaction limited by dissociative hydrogen chemisorption is 0.5; however, our observed kinetics indicate the H_2 order is ~1.0 (Table 4). The rate data can be further analyzed with double-reciprocal (Lineweaver-Burk) plots for the H_2 dependence data, shown in Figure 9A. Lineweaver-Burk plots are a common tool in enzyme kinetics; both the x- and y-intercepts represent the inverse binding constants and the maximum rate with respect to the Michaelis-Menten equation. While Equation (2) is not written in the typical Michaelis-Menten form, it is clear from Figure 9A that the y-intercepts of these plots have negative values, yielding physically meaningless values for ν_{max} (Table S2). This indicates the reaction is not adequately described by Equation 2 and the measured kinetics are inconsistent with activated homolytic H_2 activation as the RDS.

Reaction (1.3), the addition of the first Au(H) to Au(HCCR), was also considered as a possible RDS. The maximum H_2 reaction order was found to be 0.5, SI Equation (S1.2.10). Therefore, the reversible addition of the first hydrogen across the alkyne bond (after activated H_2 adsorption) is not the RDS.

We also considered reductive elimination of 1-octene (1.4) as a possible RDS. The associated rate law, shown in Equation (3), was derived assuming reactions (1.1)-(1.3) are quasi-equilibrated and that the site balance included Au, Au(HCCR), Au(H), and Au(H_2CC^*R). The full derivation is in the SI.

$$\nu_{rxn} = \frac{k_4 K_3 K_{H_2} P_{H_2} K_{HCCR} P_{HCCR}[Au]_T}{\left(1 + K_{H_2}^{0.5} P_{H_2}^{0.5} + K_{HCCR} P_{HCCR}\right)^2} \tag{3}$$

Although the rate law could be consistent with the observed kinetics, the ~0th reaction order in 1-octyne over a wide range of 1-octyne partial pressures suggests octyne binding to Au is likely strong such that the Au surface is largely saturated with 1-octyne. This is further supported by the DFT calculations (Table 3) and the coverage dependent binding energies given in Table S4. Under these limiting conditions, the denominator of (3) is dominated by $K_{HCCR}P_{HCCR}$ and the full rate law reduces to Equation (4), which is first order in H_2 and inversely proportional to 1-octyne.

$$\nu_{rxn} = \frac{k_4' K_3 K_{H_2}' P_{H_2}[Au]_T}{K_{HCCR} P_{HCCR}} \tag{4}$$

This derived mechanism is consistent with the experimental H_2 reaction orders (Table 4), the Lineweaver-Burk plot (Figure 9B and Table S4), and with the literature.[19,23] The rate law also predicts strong inhibition by 1-octyne due to the strong metal-alkyne bonding to the active sites; however, the experimental results indicate the reaction is largely insensitive to 1-octyne

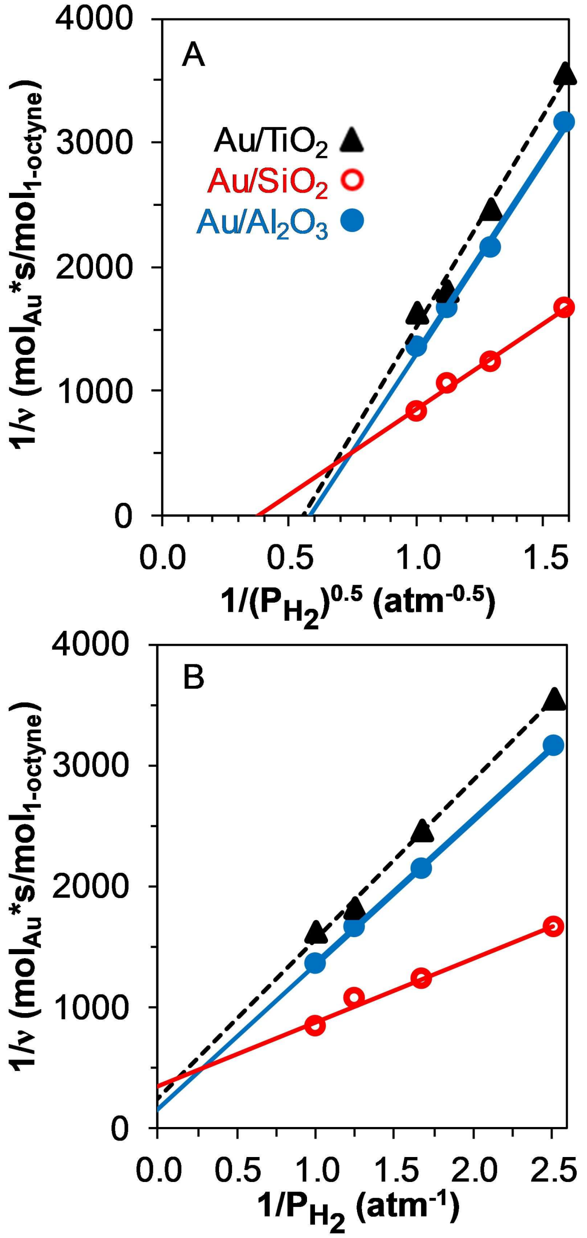

Figure 9. Lineweaver-Burk plots for Au catalysts. The order of hydrogen was fitted to 0.5 (A) and 1.0 (B). Conditions: 20–50 mL/min H_2, 20 Pa 1-octyne, 60 °C.

pressure. The Horiuti-Polanyi mechanism shown in Scheme 1, as traditionally applied, is therefore inconsistent with the combination of our observed kinetics and conclusion of strong alkyne binding to Au. A modified mechanism may be better able to explain the experimental results.

We considered an additional possibility based on Cortright and Dumesic's mechanistic investigation of ethylene hydrogenation on Pt. Under some conditions, this reaction shows similar kinetics to alkyne hydrogenation over Au (~1st order kinetics in H_2 and ~0th order kinetics in the hydrocarbon).[7] Cortright and Dumesic postulated that, while the surface was largely saturated with hydrocarbons, H_2 is small enough to access sites not available to ethylene and described these as "non-competitive" H_2 adsorption sites.[7] This mechanism can also be considered to be a description of the S-site, postulated by Boudart.[70] In the 1-octyne/Au system, the hydrocarbon layer may be sufficiently porous or loosely packed to allow for some hydrogen adsorption on the metal. We note this interpretation holds regardless of whether H_2 adsorption sites are considered to be at the metal-support interface, away from the interface on the metal surface, or both.

We present this mechanism in Scheme 2. The Au_A sites adsorb hydrogen, but not 1-octyne (2.1), while 1-octyne adsorbs on Au_B sites (2.2). Reactions (2.3) and (2.4) are analogous to reactions (1.3) and (1.4). As in the H–P mechanism, if steps (2.1) or (2.3) are rate-determining, the reaction can be at most half order in H_2. If step (2.4) is rate-determining, and steps (2.1)–(2.3) are treated as quasi-equilibrated, the resulting derived rate law is shown in Equation (5).

$$H_2 + 2Au_A \overset{K_{H_2}}{\leftrightarrow} 2Au_A(H) \quad (2.1)$$

$$HCCR + Au_B \xleftrightarrow{K_{HCCR}} Au_B(HCCR) \quad (2.2)$$

$$Au_A(H) + Au_B(HCCR) \overset{K_3}{\leftrightarrow} Au_B(H_2CC^{*}R) + Au_A \quad (2.3)$$

$$Au_A(H) + Au_B(H_2CC^{*}R) \overset{k_4}{\rightarrow} H_2CCHR + Au_A + Au_B \quad (2.4)$$

Scheme 2. Mechanism for 1-octyne hydrogenation using separate sites for H_2 activation (Au_A) and 1-octyne adsorption/reaction (Au_B). HCCR is 1-octyne and H_2CC^*R is partially-hydrogenated 1-octyne.

$$\nu_{rxn}=\frac{k_4K_3K_{H_2}P_{H_2}K_{HCCR}P_{HCCR}[Au_A]_T[Au_B]_T}{(1+K_{H_2}^{0.5}P_{H_2}^{0.5})(1+K_{HCCR}P_{HCCR})} \quad (5)$$

The denominator of (5) contains site balance terms for the H_2 activation sites (Au_A) and 1-octyne adsorption/reaction sites (Au_B). Since 1-octyne is ~0th order, the Au_B sites are likely saturated, and $K_{HCCR}P_{HCCR} \gg 1$. Chemisorption experiments have shown the H_2 adsorption capacity of Au to be relatively low (~30-60 mmol H_2/mol Au),[71] and H_2 binding to be weak.[61] Therefore under the conditions of our experiments, $K_{H_2}^{0.5}P_{H_2}^{0.5} \ll 1$ in the denominator of Equation (5), and the rate law reduces to Equation (6). This mechanism is consistent with the observed kinetics and Figure 9B (under this interpretation of the kinetic data, ν_{max} is equal to $k_4^{'}K_3K_{H_2}^{'}[Au_A]_T[Au_B]_T$).

$$\nu_{rxn}=k_4^{'}K_3K_{H_2}^{'}P_{H_2}[Au_A]_T[Au_B]_T \quad (6)$$

We further evaluated the viability of this mechanism with DFT calculations, examining the effects of 1-propyne coverage on the energy change of dissociative H_2 adsorption (see SI for complete details). Compared to H_2 chemisorption on the clean Au_{10}/TiO_2 cluster model ($\Delta E = +57$ kJ/mol), Table S22 shows that the dissociative adsorption energy varies within ±10% up to two pre-adsorbed 1-propyne molecules. When a third 1-

propyne molecule is pre-adsorbed, H_2 chemisorption becomes more endothermic and reaches a value of $\Delta E = +82$ kJ/mol. These values are generally consistent with previously reported values for a Au nanorod model on TiO_2.[61] Moreover, dissociative H_2 adsorption to Au is endothermic, suggesting low hydrogen coverage on Au regardless of the activation mechanism.

While the majority of the literature claims H_2 activation is rate-limiting, the observed kinetics are more consistent with the reaction being limited by either the availability of noncompetitive H_2 activation sites or the reductive elimination of 1-octene. Both of these elementary steps could be effectively limited by hydrogen coverage. Surprisingly, electronic support effects on alkyne hydrogenation rates over these catalysts are relatively small. It is not clear if this indicates that H_2 activation occurs away from the interface at low-coordinated Au sites, or if the kinetic relevance of the subsequent reaction steps simply mitigates any inherent support effects.

Evaluation of Heterolytic H_2 Activation Mechanisms

There is considerable evidence suggesting the lowest barrier H_2 activation sites on Au catalysts reside at the Au-MO_x interface (MSI). Indeed, the MSI is thought to be important for several reactions, including CO oxidation,[60,72] H_2 oxidation,[61,73] water-gas shift,[74] and selective propane oxidation.[75] In their early work on hydrogen activation, Haruta's group found H_2/D_2 exchange rates correlated strongly with the MSI area.[28] Heterolytic H_2 activation mechanisms have been proposed to take place at these interface sites.[61,73] Our recent study on H_2 oxidation found that, in the presence of Ti–OH, the fastest H_2 activation pathway was via heterolytic activation at the MSI, resulting in a formal hydride developing on the Au and a proton migrating to the support.[61] Similar heterolytic H_2 activation mechanisms have been proposed previously to explain Haruta's H_2/D_2 equilibration work[28,76] and Sun *et al.*'s DFT calculations.[77]

The Rossi group recently reported that phenylacetylene partial hydrogenation occurs via heterolytic H_2 activation on Au modified with an N-functionalized base.[78] A kinetic isotope effect of 2.7 was measured along with a Hammett plot with a negative slope.[78] The 1-octyne hydrogenation kinetics we observe are also consistent with this Hammett study if alkene reductive elimination or proton transfer to a formal carbanion is rate determining. While their study did not strictly examine chemistry at the MSI, Rossi's studies indicate that reaction mechanisms involving heterolytic H_2 activation can also be consistent with reaction kinetics that are first order in H_2.

The first order dependence on H_2 pressure in 1-octyne hydrogenation could be consistent with any reaction mechanism that invokes heterolytic H_2 activation at the MSI as the rate determining step. However, H_2 oxidation is considerably faster than 1-octyne hydrogenation, so the two reactions do not necessarily proceed via the same hydrogen activation pathway. In H_2 oxidation, water poisons the fast H_2 activation sites at the MSI; it is probable that the alkynes, which also adsorb onto the supports, also block some of the MSI sites. The kinetic data are therefore consistent with two possible explanations for the slower alkyne hydrogenation reaction: (i) H_2 activation proceeds through heterolytic activation, but relatively few MSI sites are available due to adsorption of the alkyne both on the support and on the Au MSI sites and (ii) the MSI sites are poisoned so strongly that slower heterolytic H_2 activation occurs on Au sites away from the MSI. Both of these interpretations are consistent with the non-competitive H_2 adsorption mechanism. While not conclusive, the relatively small support effect suggests that the latter explanation may be more likely. Further studies are underway to examine these possibilities in more detail.

Conclusions

Oleylamine-capped Au colloids were used as precursors to prepare active Au alkyne partial hydrogenation catalysts with Au particles about 3 nm in diameter. The consistent particle size across all the supports allowed for a quantitative evaluation of the support effects. The Au catalysts also showed high selectivity, with alkene selectivity exceeding 90% even at greater than 90% conversion. Reaction orders and apparent activation energies were also very similar across all the catalysts prepared from colloids, suggesting a common reaction mechanism. The observed rate constants over the colloidal catalysts varied by only a factor of two at 60 °C, indicating electronic influence from the support is relatively small.

Alkyne adsorption onto the catalysts was probed with both FTIR spectroscopy and DFT, revealing two types of hydrogen bonding interactions between the alkyne and the support: (i) between the triple bond and acidic support protons, and (ii) between the terminal alkyne C–H and more basic surface – oxo or – hydroxyl groups. These interactions were similar for the Al_2O_3, TiO_2, and SiO_2 supports. DFT calculations with 1-propyne indicate strong alkyne adsorption on Au sites, with the strongest adsorption sites at the metal-support interface.

We evaluated several alkyne hydrogenation mechanisms, including the Horiuti-Polanyi mechanism. Though the Horiuti-Polanyi mechanism is commonly invoked, the kinetic data were inconsistent with its traditional interpretation. Traditionally invoked homolytic H_2 activation (dissociative chemisorption) could not be the rate-determining step in any of the considered mechanisms, although the overall rate is likely limited by hydrogen coverage. The mechanism most consistent with the kinetic data involved noncompetitive H_2 adsorption on an alkyne covered Au surface. Similar to the mechanism Cortright and Dumesic proposed for alkene hydrogenation over Pt, this mechanism assumes that the alkyne layer is porous enough to allow the much smaller H_2 access to the Au surface.

Experimental

Materials

Gold(III) chloride trihydrate was prepared by dissolving a gold coin (99.99% Au) in aqua regia. 1,2,3,4-tetrahydronaphthalene (tetralin, 99%), oleylamine (>98%), acetone (99.5% reagent grade), and borane tert-butylamine (97%) were purchased from Sigma-Aldrich. Commercial supports included Al_2O_3 (Sasol), SiO_2 (Davicat), and P-25 TiO_2 (Degussa). Commercial catalysts included 1.0 wt. % Au/TiO_2 from Haruta Gold International (HGI) and 0.3 wt.% Pd/Al_2O_3 from Vanguard Catalyst. All gases were ultra-high purity grade (Praxair).

Catalyst Synthesis by Colloidal Methods

The synthesis of colloidal Au NP's was adapted from Peng *et al.*[49] All syntheses were performed under a N_2 atmosphere using standard Schlenk techniques. Glassware was cleaned with aqua regia prior to use. Gold(III) chloride trihydrate (240 mg) was dissolved in a mixture of 24 mL tetralin and 24 mL oleylamine in a 250 mL 3-neck round bottom flask. The flask was covered in aluminum foil and purged with N_2 three times. The solution was magnetically stirred at 800 rpm and heated to 40 °C in a circulating water bath.

Nucleation was initiated in the absence of light by rapidly injecting the reducing solution (105 mg of borane tert-butylamine, 2.4 mL tetralin, and 2.4 mL oleylamine) with a pressure equalizing funnel. The reaction proceeded for 1 h. The Au NPs were then precipitated by adding 60 mL of acetone. The solution was centrifuged at 8500 rpm for 8 min and then redispersed in hexane. After 5 min, the NPs were filtered, suspended in hexane solution, and divided into equal portions for deposition.

Commercial supports were calcined at 500 °C in a static air furnace for 16 h prior to use. Approximately 0.5 to 2.0 g of support was placed in a 50 mL Schlenk flask under flowing N_2. The Au NP solution was added dropwise while magnetically stirred at 600 rpm. The catalysts were agitated overnight in the absence of light and then thoroughly rinsed with acetone over a fritted glass filter. The catalysts were dried in air, poured into sample bottles, and stored in the dark.

The capping ligands were removed from the supported NPs prior to use. The catalyst was loaded into a tube furnace and treated under flowing H_2/N_2 (100 mL/min, 50% v/v). The furnace was ramped to 120 °C, held for 30 min, ramped to 300 °C, held for 2 h, and then cooled. All temperature ramps were 5 °C/min.

Characterization Methods

Transmission electron microscopy (TEM) images were collected on a FEI Talos equipped with HAADF (high angle annular dark field) and superX EDS (energy dispersive X-ray spectroscopy) at an accelerating voltage of 200 kV. The supported Au catalysts were dispersed in ethanol and drop cast on a lacey carbon film (Electron Microscopy Science Inc.) for TEM imaging. The particle size distribution was determined using ImageJ software.

Powder X-ray diffraction (XRD) patterns were collected on a PANalytical Empyrean diffractometer with Cu K_α radiation at 45 kV and 40 mA. Fixed slit para-focusing geometry was utilized with 0.04 radians soller slits, 10 mm beam mask, a 0.25° divergence and a 0.5° anti-scatter slit on the incidence side. Divergent optics included a 0.25° anti-scatter slit, 0.04 radians soller slits, and a nickel filter. A PIXcel detector in 1D scanning mode with PSD length of 3.35° was used.

N_2 physisorption was performed on a Micromeritics ASAP 2020. Approximately 250 mg of either catalyst or support was degassed at 200 °C for 1 h at 10 μmHg (capping ligands were removed from the colloidal catalysts *ex-situ* prior to the degassing step using the previously described procedure). The porosimetry was conducted at 77 K; surface area was calculated by the BET method. Elemental compositions were determined by inductively coupled plasma – optical emission spectroscopy (ICP-OES). Approximately 60 mg of each catalyst was digested in 10 mL aqua regia. The suspension was heated to 50 °C and vigorously stirred until all solids were dissolved. 1 mL of dissolved catalyst solution was diluted with 9 mL deionized water and then tested with a Varian 720-ES ICP-OES.

Fourier-transform infrared spectroscopy (FTIR) studies were conducted on a Nexus 470 (transmission mode, 4 cm^{-1} resolution, 128 scans). Approximately 30 mg of either catalyst or support were pressed into a 13 mm diameter wafer using a hydraulic press. Wafers were pressed at 5 metric tons for 0.5–3.0 min and then placed into a 22 mm outer diameter sample cell. The cell was placed into a closed stainless steel vessel with continuous gas flow, KBr windows, a heater, and a thermocouple. Catalysts were treated both *ex-situ* and *in-situ* with the previously described method to remove capping ligands. Background spectra were collected once the cell returned to room temperature. 1-Octyne adsorption experiments were performed by bypassing 50 mL/min of N_2 through a 1-octyne bubbler at room temperature (97%, Aldrich). After 5 min, the bypass valve was closed and a sample spectrum was immediately collected. The spectrum was further processed by subtraction of the 1-octyne gas-phase spectrum.

Density Functional Theory Calculations

The adsorption of alkynes to both Au NPs and TiO_2 was modeled using density functional theory (DFT). Plane wave based DFT calculations with periodic boundary conditions were performed using the Vienna Ab Initio Simulation Package (VASP).[79–81] The BEEF-vdW functional was used to describe the exchange and correlation energies.[79–82] The projector augmented wave (PAW) method was used to approximate the core electronic structure.[83,84] A plane wave energy cutoff of 400 eV was employed; spin polarization was found to be unnecessary.

A 10×10×10 Å simulation box for 1-propyne and 20×20×20 Å simulation box for 1-octyne was used while calculating the energies of gas phase molecules. Brillouin zone sampling was restricted to the Γ point for the gas phase species. Gaussian smearing with $k_bT = 0.01$ eV was used while calculating gas phase energy. The geometry of gas phase species was optimized using a force convergence criterion of 0.01 eV/Å. For bulk and slab models, we employed Gaussian smearing with a Fermi temperature of $k_bT = 0.1$ eV and the total energy was extrapolated to $k_bT = 0.0$ eV. Residual forces on equilibrium geometries were converged to below 0.05 eV/Å. The reaction energy for the bulk oxidation from Ti_2O_3 to TiO_2 was reproduced within an error of 0.04 eV with this arrangement. The computationally optimized lattice constants are a = 4.654 Å, a/c = 1.561 for TiO_2. These values are in good agreement with experimentally observed lattice constants of a = 4.682 Å, a/c = 1.574 for TiO_2.[85] For slab models, the Brillouin zone was sampled with a 3×2×1 Monkhorst-Pack k-point mesh and a dipole correction was applied to electrostatic potential in the z-direction. Vibrational analysis was performed with Atomic Simulation Environment (ASE) module in the harmonic oscillator approximation with a displacement of 0.01 Å along each positive and negative Cartesian direction.[86,87]

Measurement of 1-octyne Hydrogenation Kinetics

Approximately 5–7 mg of catalyst was diluted in 1.0 g SiC and loaded into a 10 mm OD borosilicate reactor. The capping ligands were removed by the heat treatment (described earlier); gas flow rates were controlled with rotameters. The reactor was cooled to 55 °C, the N_2 was shut off, and the H_2 was set to 10 mL/min. The H_2 was then bubbled through a two-stage saturator in order to ensure a consistent feed pressure of 1-octyne. The first stage was a closed vessel with liquid-phase 1-octyne at room temperature. The second stage was a closed condenser packed with glass beads and cooled to −20 °C; the second stage condensed excess 1-octyne and ensured a consistent feed pressure of 1-octyne. The feed gas was then diluted to 50 mL/min with additional H_2. The gas hourly space velocity (GHSV), based on the total mass of catalyst and SiC diluent, was ~9700 h^{-1}. The initial 1-octyne pressure was ~20 Pa (~ 200 ppm).

Light-off curves were measured by ramping the reactor temperature from 55 °C to 200 °C at a rate of 0.67 °C/min. Product gases were analyzed by an in-line gas chromatograph (SRI 8610 C) equipped with a flame ionization detector (GC/FID). A 1 m packed silica column was maintained at 240 °C for the entire test. Chromatograms were collected every 15 min (~10 °C).

Arrhenius plots and 1-octyne order plots were measured sequentially with a fresh catalyst sample. The catalyst loading and ligand removal steps were the same as the light-off curves. Data for the Arrhenius plots were collected at a reactor temperature between 45–60 °C. Reaction order plots for 1-octyne were measured at 60 °C while the temperature of the 1-octyne condenser was increased from −20 °C to 10 °C (20–200 Pa). Hydrogen order plots were generated with fresh catalyst at a reactor temperature of 60 °C, adjusting the H_2 flow and balancing with N_2 (40–100 vol.% H_2).

Acknowledgements

J.E.B, N.S.D., A.H., C.S.G., E.R.H, W.C.M, Z.C., R.M.R. and B.D.C. thank the National Science Foundation for funding. K.B.S.K. and L.C.G. also thank the NSF: CHE-CAT #1465184 and CBET #1803769. Z. C. and R. M. R. acknowledge partial support of this work from the U.S. Department of Energy, Office of Science, Office of Basic Energy Sciences Catalysis Science program, under Award DE-SC0016192. We thank Gary Gildert (Vanguard Catalyst) for supplying the Pd/Al_2O_3 *catalyst, and Prof. Chris Pursell (Trinity University) for helpful discussions and experimental expertise. The computational work used the Extreme Science and Engineering Discovery Environment (XSEDE) clusters Stampede/Stampede 2 at the Texas Advanced Computing Center (TACC) and Comet at the San Diego Supercomputing Center through allocation TG-CHE140109. High performance computational resources at the University of Houston are supported through an MRI award from the National Science Foundation (ACI-1531814), the Center of Advanced Computing and Data Science (CACDS), and the Research Computing Center (RCC). Finally, we thank the following undergraduate researchers from Trinity University for experimental assistance: Todd Whittaker, Stephen Thai, and Daniel Elizondo.*

Conflict of Interest

The authors declare no conflict of interest.

Keywords: Hydrogenation · Alkynes · Gold · Supported Catalysts · Reaction Mechanisms

[1] A. Borodziński, G. C. Bond, *Catal. Rev.* **2006**, *48*, 91–144.
[2] A. Borodziński, G. C. Bond, *Catal. Rev.* **2008**, *50*, 379–469.
[3] J. A. Lopez-Sanchez, D. Lennon, *Appl. Catal. A* **2005**, *291*, 230–237.
[4] A. Hugon, L. Delannoy, C. Louis, *Gold Bull.* **2008**, *41*, 127–138.
[5] G. Vilé, J. Pérez-Ramírez, *Nanoscale* **2014**, *6*, 13476–13482.
[6] S. A. Nikolaev, N. A. Permyakov, V. V. Smirnov, A. Y. Vasil'kov, S. N. Lanin, *Kinet. Catal.* **2010**, *51*, 288–292.
[7] R. D. Cortright, S. A. Goddard, J. E. Rekoske, J. A. Dumesic, *J. Catal.* **1991**, *127*, 342–353.
[8] M. Neurock, R. A. van Santen, *J. Phys. Chem. B* **2000**, *104*, 11127–11145.
[9] B. Yang, R. Burch, C. Hardacre, G. Headdock, P. Hu, *ACS Catal.* **2012**, *2*, 1027–1032.
[10] F. Studt, F. Abild-Pedersen, T. Bligaard, R. Z. Sørensen, C. H. Christensen, J. K. Nørskov, *Science.* **2008**, *320*, 1320.
[11] J. Liu, J. Shan, F. R. Lucci, S. Cao, E. C. H. Sykes, M. Flytzani-Stephanopoulos, *Catal. Sci. Technol.* **2017**, *7*, 4276–4284.
[12] B. V. A. , Y. V. , L. Anish, S. A. P. , V. C. P. , *ChemistrySelect* **2016**, *1*, 140–146.
[13] V. Gianvito, A. Davide, N. Maarten, C. Zupeng, D. Dariya, A. Markus, L. Núria, P.-R. Javier, *Angew. Chem. Int. Ed.* **2015**, *54*, 11265–11269; *Angew. Chem.* **2015**, *127*, 11417–11422.
[14] P. Concepción, S. García, J. C. Hernández-Garrido, J. J. Calvino, A. Corma, *Catal. Today* **2016**, *259*, 213–221.
[15] G. Kyriakou, M. B. Boucher, A. D. Jewell, E. A. Lewis, T. J. Lawton, A. E. Baber, H. L. Tierney, M. Flytzani-Stephanopoulos, E. C. H. Sykes, *Science.* **2012**, *335*, 1209.
[16] M. B. Boucher, B. Zugic, G. Cladaras, J. Kammert, M. D. Marcinkowski, T. J. Lawton, E. C. H. Sykes, M. Flytzani-Stephanopoulos, *Phys. Chem. Chem. Phys.* **2013**, *15*, 12187–12196.
[17] H. Yan, H. Cheng, H. Yi, Y. Lin, T. Yao, C. Wang, J. Li, S. Wei, J. Lu, *J. Am. Chem. Soc.* **2015**, *137*, 10484–10487.
[18] T. V. Choudhary, C. Sivadinarayana, A. K. Datye, D. Kumar, D. W. Goodman, *Catal. Lett.* **2003**, *86*, 1–8.
[19] J. Jia, K. Haraki, J. N. Kondo, K. Domen, K. Tamaru, *J. Phys. Chem. B* **2000**, *104*, 11153–11156.
[20] Y. Segura, N. López, J. Pérez-Ramírez, *J. Catal.* **2007**, *247*, 383–386.
[21] B. Hammer, J. K. Norskov, *Nature.* **1995**, *376*, 238.
[22] A. C. Gluhoi, J. W. Bakker, B. E. Nieuwenhuys, *Catal. Today* **2010**, *154*, 13–20.
[23] Y. Azizi, C. Petit, V. Pitchon, *J. Catal.* **2008**, *256*, 338–344.
[24] X. Yan, J. Wheeler, B. Jang, W.-Y. Lin, B. Zhao, *Appl. Catal. A* **2014**, *487*, 36–44.
[25] N. Masoud, L. Delannoy, H. L. Schaink, A. M. J. Van der Eerden, J.-W. de Rijk, T. A. G. Silva, D. Banerjee, J. D. Meeldijk, K. P. de Jong, C. Louis, P. E. de Jongh, *ACS Catal.* **2017**, *7*, 5594–5603.
[26] E. Bus, J. T. Miller, J. A. van Bokhoven, *J. Phys. Chem. B* **2005**, *109*, 14581–14587.
[27] X. Yan, J. Bao, C. Yuan, J. Wheeler, W.-Y. Lin, R. Li, B. W. L. Jang, *J. Catal.* **2016**, *344*, 194–201.
[28] T. Fujitani, I. Nakamura, T. Akita, M. Okumura, M. Haruta, *Angew. Chem. Int. Ed.* **2009**, *121*, 9679–9682.
[29] G. Kumar, L. Tibbitts, J. Newell, B. Panthi, A. Mukhopadhyay, R. M. Rioux, C. J. Pursell, M. Janik, B. D. Chandler, *Nat. Chem.* **2018**, *10*, 268.
[30] M. Okumura, T. Akita, M. Haruta, *Catal. Today* **2002**, *74*, 265–269.
[31] S. Schimpf, M. Lucas, C. Mohr, U. Rodemerck, A. Brückner, J. Radnik, H. Hofmeister, P. Claus, *Catal. Today* **2002**, *72*, 63–78.
[32] C.-J. Jia, F. Schüth, *Phys. Chem. Chem. Phys.* **2011**, *13*, 2457–2487.
[33] B. J. Auten, H. Lang, B. D. Chandler, *Appl. Catal. B* **2008**, *81*, 225–235.
[34] B. D. Chandler, J. D. Gilbertson, in *Nanopart. Catal.* (Ed.: D. Astruc), Wiley-VCH, Weinheim, **2008**, pp. 129–156.
[35] A. Singh, B. D. Chandler, *Langmuir* **2005**, *21*, 10776–10782.
[36] B. Donoeva, P. E. de Jongh, *ChemCatChem* **2018**, *10*, 989–997.
[37] F. Porta, L. Prati, M. Rossi, S. Coluccia, G. Martra, *Catal. Today* **2000**, *61*, 165–172.
[38] F. Porta, L. Prati, M. Rossi, G. Scari, *J. Catal.* **2002**, *211*, 464–469.
[39] S. Kunz, E. Iglesia, *J. Phys. Chem. C* **2014**, *118*, 7468–7479.
[40] A. M. Landry, E. Iglesia, *J. Catal.* **2016**, *344*, 389–400.
[41] H. Lang, R. A. May, B. L. Iversen, B. D. Chandler, *J. Am. Chem. Soc.* **2003**, *125*, 14832–14836.

[42] H. Lang, S. Maldonado, K. J. Stevenson, B. D. Chandler, *J. Am. Chem. Soc.* **2004**, *126*, 12949–12956.
[43] R. W. J. Scott, C. Sivadinarayana, O. M. Wilson, Z. Yan, D. W. Goodman, R. M. Crooks, *J. Am. Chem. Soc.* **2005**, *127*, 1380–1381.
[44] B. D. Chandler, J. D. Gilbertson, in *Top. Organomet. Chem.: Dendrimer Catalysis* (Ed.: L. Gade), Springer-Verlag, Berlin **2006**, pp. 97–120.
[45] C. A. Witham, W. Huang, C.-K. Tsung, J. N. Kuhn, G. A. Somorjai, F. D. Toste, *Naure. Chem.* **2010**, *2*, 36–41.
[46] N. Zheng, G. D. Stucky, *J. Am. Chem. Soc.* **2006**, *128*, 14278–14280.
[47] C. G. Long, J. D. Gilbertson, G. Vijayaraghavan, K. J. Stevenson, C. J. Pursell, B. D. Chandler, *J. Am. Chem. Soc.* **2008**, *130*, 10103–10115.
[48] R. J. Korkosz, J. D. Gilbertson, K. S. Prasifka, B. D. Chandler, *Catal. Today* **2007**, *122*, 370–377.
[49] S. Peng, Y. Lee, C. Wang, H. Yin, S. Dai, S. Sun, *Nano Res.* **2008**, *1*, 229–234.
[50] B. D. Chandler, C. G. Long, J. D. Gilbertson, G. Vijayaraghavan, K. J. Stevenson, C. J. Pursell, *J. Phys. Chem. C* **2010**, *114*, 11498–11508.
[51] M. Breysse, P. Afanasiev, C. Geantet, M. Vrinat, *Catal. Today* **2003**, *86*, 5–16.
[52] X. Y. Liu, A. Wang, T. Zhang, C.-Y. Mou, *Nano Today* **2013**, *8*, 403–416.
[53] T. Zheng, J. He, Y. Zhao, W. Xia, J. He, *J. Rare Earths* **2014**, *32*, 97–107.
[54] T. Mitsudome, K. Kaneda, *Green Chem.* **2013**, *15*, 2636–2654.
[55] S. D. Jackson, N. J. Casey, *J. Chem. Soc. Faraday Trans.* **1995**, *91*, 3269–3274.
[56] R. G. Greenler, D. R. Snider, D. Witt, R. S. Sorbello, *Surf. Sci.* **1982**, *118*, 415–428.
[57] H. A. Pearce, N. Sheppard, *Surf. Sci.* **1976**, *59*, 205–217.
[58] S. Gautam, A. D. Sarkar, *Phys. Chem. Chem. Phys.* **2016**, *18*, 13830–13843.
[59] E. Es-sebbar, A. Jolly, Y. Benilan, A. Farooq, *J. Mol. Spectrosc.* **2014**, *305*, 10–16.
[60] J. Saavedra, H. A. Doan, C. J. Pursell, L. C. Grabow, B. D. Chandler, *Science* **2014**, *345*, 1599–1602.
[61] T. Whittaker, S. K. Kanchari Bavajigari, C. Peterson, M. N. Pollock, L. C. Grabow, B. D. Chandler, *J. Am. Chem. Soc.* **2018**, *140*, 16469–16487.
[62] A. Sárkány, *React. Kinet. Catal. Lett.* **2009**, *96*, 43–54.
[63] A. Corma, M. J. Sabater, in *Environmental Catalysis over Gold-Based Materials* (Eds. G. Avgouropoulos, T. Tabakova), The Royal Society of Chemistry, Cambridge **2013**, pp. 146–200.
[64] M. Pan, D. W. Flaherty, C. B. Mullins, *J. Phys. Chem. Lett.* **2011**, *2*, 1363–1367.
[65] M. Pan, A. J. Brush, Z. D. Pozun, H. C. Ham, W.-Y. Yu, G. Henkelman, G. S. Hwang, C. B. Mullins, *Chem. Soc. Rev.* **2013**, *42*, 5002–5013.
[66] M. Boronat, P. Concepción, A. Corma, *J. Phys. Chem. C* **2009**, *113*, 16772–16784.
[67] B. Yang, R. Burch, C. Hardacre, P. Hu, P. Hughes, *Catal. Sci. Technol.* **2017**, *7*, 1508–1514.
[68] J. A. Delgado, O. Benkirane, C. Claver, D. Curulla-Ferre, C. Godard, *Dalton Trans.* **2017**, *46*, 12381–12403.
[69] A. Hugon, L. Delannoy, C. Louis, *Gold Bull.* **2009**, *42*, 310–320.
[70] M. Boudart, G. Djega-Mariadassou, *Kinetics of Heterogeneous Catalytic Reactions*, Princeton University Press, Princeton, **1984**, pp. 180–193.
[71] M. Li, L. Collado, F. Cárdenas-Lizana, M. A. Keane, *Catal. Lett.* **2018**, *148*, 90–96.
[72] J. Saavedra, T. Whittaker, Z. Chen, C. J. Pursell, R. M. Rioux, B. D. Chandler, *Nature. Chem.* **2016**, *8*, 584.
[73] I. X. Green, W. Tang, M. Neurock, J. T. Yates, *Angew. Chem. Int. Ed.* **2011**, *50*, 10186–10189; *Angew. Chem.* **2011**, *123*, 10368–10371.
[74] M. Flytzani-Stephanopoulos, *Acc. Chem. Res.* **2014**, *47*, 783–792.
[75] Y. Y. Wu, N. A. Mashayekhi, H. H. Kung, *Catal. Sci. Technol.* **2013**, *3*, 2881–2891.
[76] B. Yang, X.-M. Cao, X.-Q. Gong, P. Hu, *Phys. Chem. Chem. Phys.* **2012**, *14*, 3741–3745.
[77] K. Sun, M. Kohyama, S. Tanaka, S. Takeda, *J. Phys. Chem. C* **2014**, *118*, 1611–1617.
[78] J. L. Fiorio, R. V. Gonçalves, E. Teixeira-Neto, M. A. Ortuño, N. López, L. M. Rossi, *ACS Catal.* **2018**, *8*, 3516–3524.
[79] G. Kresse, J. Hafner, *Phys. Rev. B* **1993**, *47*, 558–561.
[80] G. Kresse, J. Furthmüller, *Phys. Rev. B* **1996**, *54*, 11169–11186.
[81] G. Kresse, J. Furthmüller, *Comput. Mater. Sci.* **1996**, *6*, 15–50.
[82] J. Wellendorff, K. T. Lundgaard, A. Møgelhøj, V. Petzold, D. D. Landis, J. K. Nørskov, T. Bligaard, K. W. Jacobsen, *Phys. Rev. B* **2012**, *85*, 235149.
[83] P. E. Blöchl, *Phys. Rev. B* **1994**, *50*, 17953–17979.
[84] G. Kresse, D. Joubert, *Phys. Rev. B* **1999**, *59*, 1758–1775.
[85] V. Tripkovic, I. Cerri, T. Nagami, T. Bligaard, J. Rossmeisl, *Phys. Chem. Chem. Phys.* **2013**, *15*, 3279–3285.
[86] S. R. Bahn, K. W. Jacobsen, *Comput. Sci. Eng.* **2002**, *4*, 56–66.
[87] L. Ask Hjorth, *J. Phys. Condens. Matter* **2017**, *29*, 273002.

Manuscript received: November 16, 2018
Revised manuscript received: January 25, 2019
Accepted manuscript online: January 28, 2019
Version of record online: February 28, 2019